

Crossover from itinerant to localized magnetic excitations through the metal-insulator transition in NaOsO₃

J. G. Vale,^{1,2,*} S. Calder,^{3,†} C. Donnerer,¹ D. Pincini,^{1,4} Y. G. Shi,^{5,6} Y. Tsujimoto,⁶ K. Yamaura,^{6,7} M. Moretti Sala,⁸ J. van den Brink,⁹ A. D. Christianson,^{3,10} and D. F. McMorrow¹

¹*London Centre for Nanotechnology and Department of Physics and Astronomy, University College London, Gower Street, London, WC1E 6BT, United Kingdom*

²*Laboratory for Quantum Magnetism, École Polytechnique Fédérale de Lausanne (EPFL), CH-1015, Switzerland*

³*Quantum Condensed Matter Division, Oak Ridge National Laboratory, Oak Ridge, Tennessee 37831, USA*

⁴*Diamond Light Source, Harwell Science and Innovation Campus, Didcot, Oxfordshire, OX11 0DE, United Kingdom*

⁵*Beijing National Laboratory for Condensed Matter Physics and Institute of Physics, Chinese Academy of Sciences, Beijing 100190, China*

⁶*Research Center for Functional Materials, National Institute for Materials Science, 1-1 Namiki, Tsukuba, Ibaraki 305-0044, Japan*

⁷*Graduate School of Chemical Sciences and Engineering, Hokkaido University, North 10 West 8, Kita-ku, Sapporo, Hokkaido 060-0810, Japan*

⁸*ESRF, The European Synchrotron, 71 Avenue des Martyrs, 38043 Grenoble, France*

⁹*Institute for Theoretical Solid State Physics, IFW Dresden, D01171 Dresden, Germany*

¹⁰*Department of Physics and Astronomy, University of Tennessee, Knoxville, TN 37996, USA*

Resonant inelastic x-ray scattering (RIXS) was used to probe the electronic and magnetic excitations in NaOsO₃ through its metal-insulator transition (MIT). Whilst local electronic excitations do not change appreciably through the MIT, well-defined, low energy magnetic excitations present in the insulating state become noticeably weakened and damped upon approaching the metallic state. Concomitantly, a broad continuum of high-energy excitations develops which is well described by the magnetic fluctuations of a nearly antiferromagnetic Fermi liquid. By revealing the continuous evolution of the quasiparticle spectrum as it changes its character from localized to itinerant, our results provide unprecedented insight into the nature of the MIT in NaOsO₃.

PACS numbers: 71.30.+h, 75.25.-j

The nature of the MIT in transition metal oxides (TMOs) is of enduring interest as it represents a spectacular manifestation of competing interactions, and their effects on the most fundamental transport property of materials. Recently, considerable attention has focussed on the nature of the MIT in 5d TMOs, which have the additional ingredients of strong spin-orbit coupling and a lower degree of localization relative to their 3d counterparts [1]. New phenomenology has been revealed by experiment, including a number of MITs which are intimately entwined with the onset of magnetic order, placing them outside of the conventional Mott-Hubbard paradigm. A key and yet unsolved issue for such systems is to fully determine the nature of the magnetic quasiparticle spectrum as the electronic character evolves from itinerant to localized through the MIT.

Magnetic interactions in materials are usually defined in terms of one of two limits [2]. In the local moment (Heisenberg) limit, magnetism is assumed to arise from unpaired electrons within an atomic picture. At some temperature T , the orientation of the magnetic moments varies, but their magnitude remains fixed at the $T = 0$ value. Consequently only the transverse component of the local spin density fluctuation (LSF) $\chi^\pm(q, \omega)$ is important. This gives rise to collective spin wave excitations and is generally applicable to magnetic insulators. At

the other extreme (itinerant or Stoner limit), the electrons and spin fluctuations are extended in real space (Thermodynamic properties of the system are governed by intraband electron-hole pair interactions, which have a degree of collective behaviour). At some temperature T , the orientation of the magnetic moments remains fixed, but their magnitude is reduced from the $T = 0$ value. In this limit, the longitudinal component $\chi^{zz}(q, \omega)$ and the temperature dependence of the LSF are important. Between these two limits, one typically observes Landau damping of spin waves by intraband particle-hole excitations. Damping is more prevalent at large momentum transfers q since there are a greater number of available states for the corresponding magnon to decay into. Such an effect has been observed in a number of materials, notably doped La_{2-x}Sr_xCuO₄ [3–5], and a subset of the iron pnictides [6–11]. A summary of the behaviour in the respective limits is shown schematically in Fig. 1.

Here we focus our attention upon materials which undergo continuous MITs with temperature, that are concomitant with the onset of long-ranged, commensurate antiferromagnetic order. Moreover, these MITs are not associated with any global symmetry change. Examples include some of the 5d⁵ pyrochlore iridates R₂Ir₂O₇ (R = Ln³⁺) [12, 13], plus the 5d³ osmates Cd₂Os₂O₇ [14–16], and NaOsO₃. The latter material has been pro-

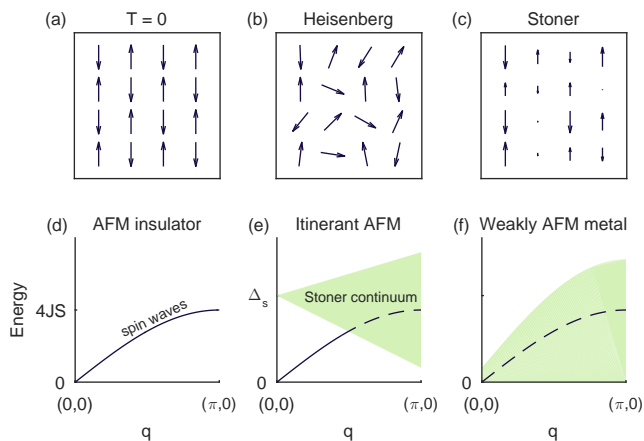


FIG. 1. Top panels: Schematic of the orientation of anti-ferromagnetically (AFM) interacting magnetic moments on a square lattice for $T = 0$, and finite temperatures in the Heisenberg or Stoner limits. Bottom panels: Excitation spectra in the Heisenberg limit, for an itinerant AFM (with critical energy scale Δ_s), and for a metal with weak AFM correlations. Dashed lines indicate damped excitations.

posed to be an example of a Slater insulator [17–21], in which the formation of antiferromagnetic order itself at $T_{\text{MI}} = 410$ K drives the formation of an insulating gap below the Néel temperature. Together with significant spin-phonon coupling [22], one observes an unprecedented connection between the magnetic, electronic, structural, and phonon degrees of freedom in NaOsO_3 .

One would thus expect the electronic and magnetic excitations to evolve correspondingly through the MIT. Optical conductivity measurements [21] reveal a continuous opening of the electronic gap with decreasing temperature $\{\Delta_g(0) = 102(3)$ meV $\}$, and an MIT in which electronic correlations play a limited role. This is consistent with an itinerant Slater picture in which interactions are mean-field like. Meanwhile previous RIXS measurements [23] showed well-defined and strongly gapped (~ 50 meV) dispersive spin-wave excitations at 300 K. This was found to be consistent with an anisotropic nearest-neighbour Heisenberg picture for the magnetic Hamiltonian, and is suggestive of localized magnetic moments. The question remains whether either the spin or electronic excitations remain coherent through the MIT, and if there is any evidence of coupling to any of the other relevant degrees of freedom present in the system.

In this Letter, we establish that in NaOsO_3 , there is a continuous progression from localized to itinerant behaviour through the MIT. This can be directly observed through the temperature and momentum dependence of the electronic and magnetic excitations. RIXS is uniquely placed as a technique which is simultaneously sensitive to the orbital, electronic, and magnetic degrees of freedom in materials. For this reason, RIXS measurements (Os L_3 edge, $E = 10.871$ keV) were performed on

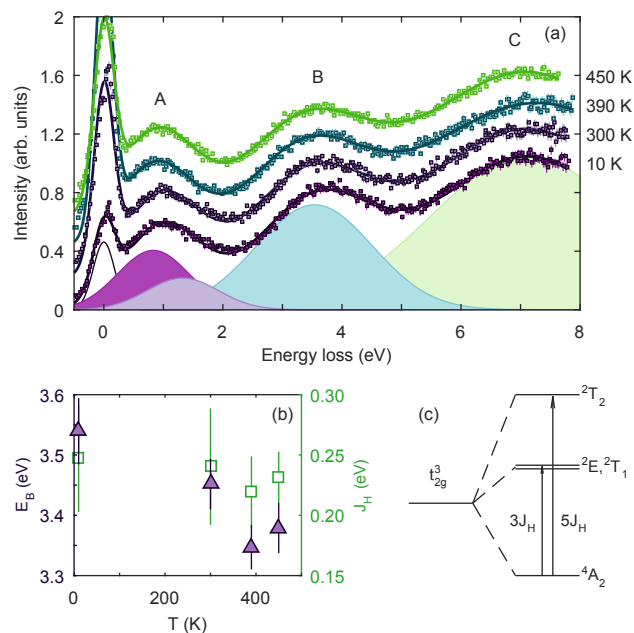


FIG. 2. (a): Orbital excitations as a function of temperature, obtained using a low resolution setup ($\Delta E = 300$ meV). The excitations are practically temperature independent. Solid lines are best fit to data by the sum of five Gaussians. Shaded peaks show the relative contributions at 10 K. (b): Fitted energy of peak B (triangles), and value of Hund's coupling J_H calculated from fitted peak positions of intra- t_{2g} excitations (peak A). (c): Low energy transitions possible in NaOsO_3 within the LS coupling limit, and assuming zero trigonal distortion.

the ID20 spectrometer at the ESRF, Grenoble. Details of the experimental setup are provided in the Supplemental Material.

We start with the orbital excitations as a function of temperature. A low resolution setup ($\Delta E = 300$ meV) was used in order to examine the orbital excitations out to large energy loss (8 eV). Selected spectra are displayed in Fig. 2(a). Just as in Ref. 23, four peaks are evident in the RIXS spectra. The peak centered at zero energy loss comprises the elastic line and other low energy features such as phonons, magnons etc. The three remaining peaks refer to excitations within the t_{2g} manifold (A), excitations from t_{2g} to e_g states (B), and ligand-to-metal charge transfer (C). This assignment follows the previous RIXS measurements [23, 24] on NaOsO_3 and $\text{Cd}_2\text{Os}_2\text{O}_7$. Figure 2(b) shows that the intensity and positions of peaks A–C appear to be essentially temperature independent. Moreover, the individual features are much broader than the instrumental resolution, indicative of a system with significant non-local character. The increased peak width with respect to the isoelectronic $\text{Ca}_3\text{LiOsO}_6$ and Ba_2YOsO_6 [25] is likely a result of the increased itineracy in NaOsO_3 . Within a simple LS -coupling model, which neglects the effects of weak octahedral distortion, peak

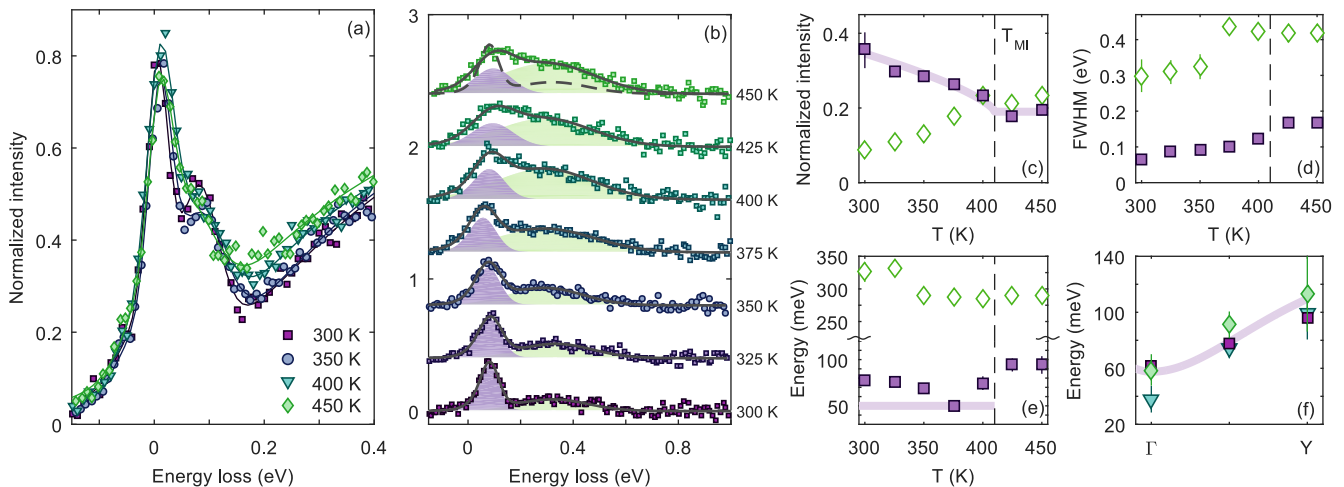


FIG. 3. Analysis of RIXS spectra collected at Γ - Y . (a): Representative low-energy RIXS spectra, each of which is normalised to the d - d excitations at 1 eV energy loss. (b): Spectra with elastic line and d - d contributions subtracted. Added are the best fit to the data (black solid line), and relative components of the magnon peak (purple) and particle-hole continuum (green). Dashed line superimposed on 450 K plot is best fit to 300 K data for comparison. (c-e): Fitted peak intensity (c), FWHM (d), and energy (e) of the two components as a function of temperature. Solid lines are guides to the eye. (f): Energy of magnon peak as function of momentum transfer and temperature. The symbols are the same as part (a). Solid line is best fit to dispersion at 300 K as determined within Ref. 23.

A is comprised of two overlapping excitations centred at $3J_H$ and $5J_H$ (Fig. 2c). We find that $J_H = 0.23(3)$ eV is temperature independent within experimental uncertainty. This compares well with previous estimates obtained from other $5d^3$ materials [24, 25]. Moreover, high resolution ($\Delta E = 56$ meV) measurements of the RIXS spectra below 2.5 eV energy loss show similar behaviour [26]. This corroborates the observation that the MIT is not driven by structural distortion, which would manifest as a variance in the electronic excitations with temperature.

We now move to the high-resolution RIXS data; the main focus of this paper. RIXS spectra were collected at three different momentum transfers as a function of temperature: Γ (4.95, 2.95, 3.95), Γ - Y (4.75, 3, 4), and Y (4.5, 3, 4). This reflects a progression from the Brillouin zone centre to the zone boundary. The point near Γ was chosen in order to avoid the weak magnetic Bragg peak at (5, 3, 4). Spectra were normalized to the intensity of the intra- t_{2g} excitations at 1 eV energy loss.

Representative RIXS spectra collected at Γ - Y are displayed in Fig. 3(a), for temperatures below and above the MIT. Data taken at Γ and Y , showing qualitatively similar behaviour, are given in the Supplemental Material. To better isolate changes to the spectra below 1 eV, they are shown with the elastic line and d - d contributions subtracted in Fig. 3(b). The spectrum at 300 K is in agreement with that given in Ref. 23, with a sharp peak evident at 60–100 meV energy loss attributable to a single magnon excitation. With increasing temperature this peak progressively weakens and broadens. Strikingly,

concurrent with the diminishing of the single magnon peak, there is a continuous increase in intensity between 0.1 and 0.6 eV, whilst there is no significant change in the d - d excitations. In order to quantify these observations further, the data were fitted with Gaussians to represent the elastic line, magnon peak, broad component centred around 300 meV, and the intra- t_{2g} excitations. The fits in the low energy portion of the RIXS spectra were corrected to take the Bose factor into account. Prior to fitting, the model lineshape was convoluted with the experimental resolution function, which had a Pearson VII functional form. This minimal model for the lineshape was used in order to reduce the number of free parameters in the fit, whilst allowing the relevant features of the data to be captured. The result of these fits at Γ - Y is plotted in Figs. 3(c)–(e). Clearly there is a significant variation of the RIXS spectra through the MIT. We turn first to consider the various aspects of the temperature dependence of the low-energy magnon spectra captured in Fig. 3, before considering the nature of the high energy continuum scattering.

We observe a weak variation in the energy of the magnon peak with temperature. Fig. 3(e) shows that the magnon appears to soften by about 20 meV between 300 K and 375 K. Similar behavior is observed at Γ . This would agree qualitatively with DFT+U calculations [27], which predict a continuous reduction of the magnetic moment through the MIT due to longitudinal spin fluctuations. Yet Fig. 3(f) shows that the magnon dispersion appears remarkably constant through the MIT – within experimental resolution. It is thus unclear whether our

observation is in fact an experimental artefact.

In general, there are two relevant mechanisms which may lead to magnon damping: spin-phonon coupling [28], and the aforementioned Landau damping by intra-band particle-hole (Stoner) excitations. It has already been shown [22] that there is a dramatic shift of the phonon modes in NaOsO₃ as a function of temperature, which the authors propose is due to coupling between the spin and lattice degrees of freedom. However spin-phonon coupling alone does not explain the observed high-temperature damping of the magnon peak at Γ . Instead we suggest that this is a direct result of Landau damping by Stoner excitations in the itinerant limit.

In order to explain the formation of the continuum scattering centred around 0.3 eV (Fig. 3(b)) as NaOsO₃ enters its high-temperature metallic phase, we considered possible mechanisms: two-magnon excitations, electronic interband particle-hole excitations, and Stoner excitations from a nascent Fermi liquid. Details of calculations to assess the contributions from the first two candidate mechanisms are considered in detail in the Supplementary Material. There we argue that neither of them provide an adequate description of the energy and wavevector dependences of the high-energy continuum evident in our data.

We instead propose that the bulk of the scattering at high temperatures results from paramagnetic spin fluctuations, with the other components only contributing weakly. The high temperature behaviour can be qualitatively modelled within a nearly antiferromagnetic Fermi liquid approach using self-consistent renormalization (SCR) theory [2]. The assumption is that the fluctuations are isotropic, which is reasonable given the similar magnitude of J_1 and J_2 . Moreover for simplicity we consider a pseudo-cubic unit cell, with a lattice constant $a = 3.80$ Å given by the Os-Os distance. Following the approach of Inosov [29] and Tucker [30], the imaginary part of the dynamic susceptibility $\chi''(\mathbf{Q}, E)$ is given by:

$$\chi''(\mathbf{Q}, E) = \frac{\chi_0 \gamma E}{E^2 + \left(\frac{\gamma a}{\xi}\right)^2 [1 + \xi^2(\mathbf{Q} - \mathbf{Q}_{\text{AFM}})^2]}, \quad (1)$$

where ξ is the spin-spin correlation length, a is the lattice constant, γ denotes the damping coefficient arising from spin decay into particle-hole excitations (related to the electronic band structure), and χ_0 is the staggered susceptibility [31]. All of these parameters are in principle dependent upon temperature. For completeness the anti-Stokes (energy gain) process has also been included; this is a factor $\exp(\hbar\omega/kT)$ weaker than the equivalent Stokes (energy loss) process. Note however that the experimental RIXS cross-section includes a number of additional contributions, which include momentum-dependent absorption and polarization effects. In our analysis we replace the equality in Eqn. 1 by a proportionality in order to reflect this phenomenologically.

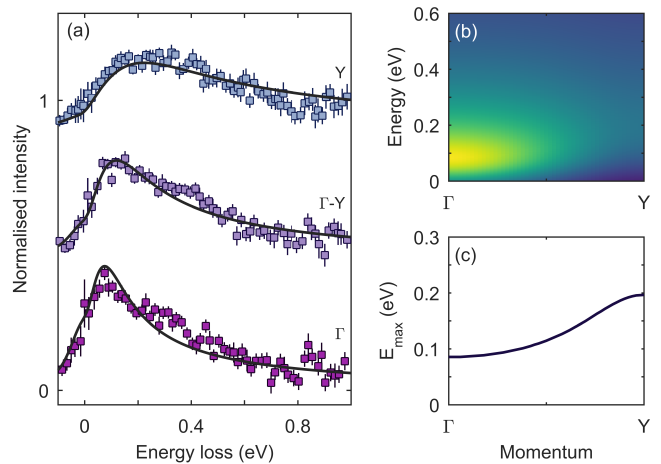


FIG. 4. Paramagnetic spin fluctuations in NaOsO₃ at 450 K for $\gamma = 50$ meV and $\xi/a = 1$. (a): Comparison of model with experimental data at various crystal momenta. For clarity the elastic line and high-energy intra- t_{2g} excitations have been subtracted. (b): Calculated $\chi''(\mathbf{Q}, E)$, with intensity scale in arbitrary units. (c): Maximum of $\chi''(\mathbf{Q}, E)$ as a function of momentum transfer.

The interplay between the correlation length and damping governs the characteristic energy of the damped excitations. We find (Fig. 4) that the experimental data is fairly well described by this simple model using $\gamma \sim 50$ meV and $\xi/a \sim 1$. These two parameters are of the same magnitude as the spin wave gap (in the Heisenberg limit), and the Os-Os bond distance respectively. Hence one can argue at 450 K that the spin fluctuations are short-ranged. We note that improvements in the quantitative agreement with the experimental data could likely be made by considering anisotropic spin fluctuations, or the effect of finite momentum resolution of the spectrometer. However, there are insufficient data to perform this robustly.

The results presented here are put into context with the previously published RIXS data [23]. We argue that at 300 K, NaOsO₃ cannot be considered as a fully localized Heisenberg antiferromagnet. This is primarily due to the significant intrinsic Os-O hybridisation [20]. Within a weak coupling theory [32], collective antiferromagnetic spin wave excitations are expected to merge into a Stoner continuum above a critical energy $\Delta_s \approx \pi k_B T_N [8\alpha^2 t / 7\zeta(3)]^{1/2}$, where $T_N = 410$ K is the Néel temperature, $t = 1 - T/T_N$, $\alpha = v_e v_h / \sqrt{4v_e v_h} \approx 1$ is a dimensionless parameter relating the electron and hole band velocities, and $\zeta(3)$ is the Riemann zeta function of the third kind. Note the mean-field temperature dependence. As $T \rightarrow T_N$, the energy scale for Δ_s decreases, meaning that the collective excitations become damped over a larger proportion of the Brillouin zone (Fig. 1(e)). Taking $\alpha = 1$, then $\Delta_s [T = 300 \text{ K}] \approx 60$ meV, which we observe is of similar magnitude to both the spin and

optical gaps ($\Delta_g \sim 80$ meV). This argument is expected to remain valid for weak electronic correlations U , and implies that the collective excitations should be (weakly) damped at all wavevectors.

In summary, we find that at 300 K, NaOsO_3 lies close to, but not within, the Heisenberg limit. The magnetic scattering is dominated by single-magnon processes, albeit with some contribution from two-magnon and interband particle-hole excitations. With increasing temperature, one observes a continuous progression towards the itinerant limit through the MIT. At 450 K, paramagnetic spin fluctuations dominate, which can be modelled successfully within a SCR picture. Similarities can be drawn with properties seen in the doped cuprates and iron pnictides as a function of temperature and carrier doping.

These observations directly map themselves onto the discussion of the proposed Slater MIT in this material. In a simple Slater theory, insulating electronic behaviour manifests concurrently with the formation of a spin-density wave (SDW) magnetic ground state below T_N . The paramagnetic spin fluctuations of a candidate SDW system have been previously shown [33] to exhibit behaviour consistent with a SCR model. The results presented here reveal the presence of magnetic correlations which require a theoretical framework beyond a mean-field type of Slater description of the MIT in NaOsO_3 . Finally we show that RIXS opens a new window on the progression of quasiparticle spectra through metal-insulator transitions.

J. G. V. thanks UCL and EPFL for financial support via a UCL Impact Studentship, and A. Princep for useful discussions. Work at UCL was supported by the Engineering and Physical Sciences Research Council (EPSRC). This research used resources at the High Flux Isotope Reactor and Spallation Neutron Source, DOE Office of Science User Facilities operated by the Oak Ridge National Laboratory. K.Y. thanks financial support from JSPS KAKENHI (15K14133 and 16H04501).

* j.vale@ucl.ac.uk

† caldersa@ornl.gov

- [1] W. Witczak-Krempa, G. Chen, Y. B. Kim, and L. Balents, *Ann. Rev. Cond. Mat. Phys.* **5**, 57 (2014).
- [2] T. Moriya, *Spin Fluctuations in Itinerant Electron Magnetism*, Springer Series in Solid-State Sciences (Springer-Verlag Berlin Heidelberg, 1985).
- [3] M. Le Tacon, G. Ghiringhelli, J. Chaloupka, M. M. Sala, V. Hinkov, M. Haverkort, M. Minola, M. Bakr, K. Zhou, S. Blanco-Canosa, C. Monney, Y. T. Song, G. L. Sun, C. T. Lin, G. M. De Luca, M. Salluzzo, G. Khaliullin, T. Schmitt, L. Braicovich, and B. Keimer, *Nature Physics* **7**, 725 (2011).
- [4] M. P. M. Dean, G. Dellea, R. S. Springell, F. Yakhov-Harris, K. Kummer, N. B. Brookes, X. Liu, Y.-J. Sun, J. Strle, T. Schmitt, L. Braicovich, G. Ghiringhelli, I. Boovi, and J. P. Hill, *Nature Materials* **12**, 1019 (2013).
- [5] C. Monney, T. Schmitt, C. E. Matt, J. Mesot, V. N. Strocov, O. J. Lipscombe, S. M. Hayden, and J. Chang, *Phys. Rev. B* **93**, 075103 (2016).
- [6] S. O. Diallo, V. P. Antropov, T. G. Perring, C. Broholm, J. J. Pulikkotil, N. Ni, S. L. Bud'ko, P. C. Canfield, A. Kreyssig, A. I. Goldman, and R. J. McQueeney, *Phys. Rev. Lett.* **102**, 187206 (2009).
- [7] J. Zhao, D. Adroja, D.-X. Yao, R. Bewley, S. Li, X. Wang, G. Wu, X. Chen, J. Hu, and P. Dai, *Nature Physics* **5**, 555 (2009).
- [8] K.-J. Zhou, Y.-B. Huang, C. Monney, X. Dai, V. N. Strocov, N.-L. Wang, Z.-G. Chen, C. Zhang, P. Dai, L. Patthey, J. van den Brink, H. Ding, and T. Schmitt, *Nature Communications* **4**, 1470 (2013).
- [9] C. Wang, R. Zhang, F. Wang, H. Luo, L. P. Regnault, P. Dai, and Y. Li, *Phys. Rev. X* **3**, 041036 (2013).
- [10] Z. Leong, W.-C. Lee, W. Lv, and P. Phillips, *Phys. Rev. B* **90**, 125158 (2014).
- [11] P. Dai, *Rev. Mod. Phys.* **87**, 855 (2015).
- [12] K. Matsuhira, M. Wakeshima, Y. Hinatsu, and S. Takagi, *J. Phys. Soc. Jpn.* **80**, 094701 (2011).
- [13] M. Nakayama, T. Kondo, Z. Tian, J. J. Ishikawa, M. Halim, C. Bareille, W. Malaeb, K. Kuroda, T. Tomita, S. Ideta, K. Tanaka, M. Matsumami, S. Kimura, N. Inami, K. Ono, H. Kumigashira, L. Balents, S. Nakatsuji, and S. Shin, *Phys. Rev. Lett.* **117**, 056403 (2016).
- [14] D. Mandrus, J. R. Thompson, R. Gaal, L. Forro, J. C. Bryan, B. C. Chakoumakos, L. M. Woods, B. C. Sales, R. S. Fishman, and V. Keppens, *Phys. Rev. B* **63**, 195104 (2001).
- [15] W. J. Padilla, D. Mandrus, and D. N. Basov, *Phys. Rev. B* **66**, 035120 (2002).
- [16] J. Yamaura, K. Ohgushi, H. Ohsumi, T. Hasegawa, I. Yamauchi, K. Sugimoto, S. Takeshita, A. Tokuda, M. Takata, M. Udagawa, M. Takigawa, H. Harima, T. Arima, and Z. Hiroi, *Phys. Rev. Lett.* **108**, 247205 (2012).
- [17] Y. G. Shi, Y. F. Guo, S. Yu, M. Arai, A. A. Belik, A. Sato, K. Yamaura, E. Takayama-Muromachi, H. F. Tian, H. X. Yang, J. Q. Li, T. Varga, J. F. Mitchell, and S. Okamoto, *Phys. Rev. B* **80**, 161104 (2009).
- [18] S. Calder, V. O. Garlea, D. F. McMorrow, M. D. Lumsden, M. B. Stone, J. C. Lang, J.-W. Kim, J. A. Schlueter, Y. G. Shi, K. Yamaura, Y. S. Sun, Y. Tsujimoto, and A. D. Christianson, *Phys. Rev. Lett.* **108**, 257209 (2012).
- [19] Y. Du, X. Wan, L. Sheng, J. Dong, and S. Y. Savrasov, *Phys. Rev. B* **85**, 174424 (2012).
- [20] M.-C. Jung, Y.-J. Song, K.-W. Lee, and W. E. Pickett, *Phys. Rev. B* **87**, 115119 (2013).
- [21] I. L. Vecchio, A. Perucchi, P. Di Pietro, O. Limaj, U. Schade, Y. Sun, M. Arai, K. Yamaura, and S. Lupi, *Scientific Reports* **3**, 2990 (2013).
- [22] S. Calder, J. H. Lee, M. B. Stone, M. D. Lumsden, J. C. Lang, M. Feyngenson, Z. Zhao, X.-Q. Yan, Y. G. Shi, Y. S. Sun, Y. Tsujimoto, K. Yamaura, and A. D. Christianson, *Nature Communications* **6**, 9916 (2015).
- [23] S. Calder, J. G. Vale, N. Bogdanov, C. Donnerer, D. Pincini, M. Moretti Sala, X. Liu, M. H. Upton, D. Casa, Y. G. Shi, Y. Tsujimoto, K. Yamaura, J. P. Hill, J. van den Brink, D. F. McMorrow, and A. D. Christianson, *Phys. Rev. B* **95**, 020413 (2017).

- [24] S. Calder, J. G. Vale, N. A. Bogdanov, X. Liu, C. Donnerer, M. H. Upton, D. Casa, A. H. Said, M. D. Lumsden, Z. Zhao, J. Q. Yan, D. Mandrus, S. Nishimoto, J. van den Brink, J. P. Hill, D. F. McMorrow, and A. D. Christianson, *Nature Communications* **7**, 11651 (2016).
- [25] A. E. Taylor, S. Calder, R. Morrow, H. L. Feng, M. H. Upton, M. D. Lumsden, K. Yamamura, P. M. Woodward, and A. D. Christianson, *Phys. Rev. Lett.* **118**, 207202 (2017).
- [26] See Supplemental Material for a discussion of modelling the orbital excitations within an intermediate coupling model.
- [27] B. Kim, P. Liu, Z. Ergönenc, A. Toschi, S. Khmelevskyi, and C. Franchini, *Phys. Rev. B* **94**, 241113 (2016).
- [28] P. Dai, H. Y. Hwang, J. Zhang, J. A. Fernandez-Baca, S.-W. Cheong, C. Kloc, Y. Tomioka, and Y. Tokura, *Phys. Rev. B* **61**, 9553 (2000).
- [29] D. Inosov, J. Park, P. Bourges, D. Sun, Y. Sidis, A. Schneidewind, K. Hradil, D. Haug, C. Lin, B. Keimer, and V. Hinkov, *Nature Physics* **6**, 178 (2010).
- [30] G. S. Tucker, R. M. Fernandes, D. K. Pratt, A. Thaler, N. Ni, K. Marty, A. D. Christianson, M. D. Lumsden, B. C. Sales, A. S. Sefat, S. L. Bud'ko, P. C. Canfield, A. Kreyssig, A. I. Goldman, and R. J. McQueeney, *Phys. Rev. B* **89**, 180503 (2014).
- [31] S. O. Diallo, D. K. Pratt, R. M. Fernandes, W. Tian, J. L. Zarestky, M. Lumsden, T. G. Perring, C. L. Broholm, N. Ni, S. L. Bud'ko, P. C. Canfield, H.-F. Li, D. Vaknin, A. Kreyssig, A. I. Goldman, and R. J. McQueeney, *Phys. Rev. B* **81**, 214407 (2010).
- [32] P. A. Fedders and P. C. Martin, *Phys. Rev.* **143**, 245 (1966).
- [33] W. Bao, C. Broholm, J. M. Honig, P. Metcalf, and S. F. Trevino, *Phys. Rev. B* **54**, R3726 (1996).

SUPPLEMENTAL MATERIAL

J. G. Vale, S. Calder, C. Donnerer, D. Pincini, Y. G. Shi, Y. Tsujimoto, K. Yamaura, M. Moretti Sala, J. van den Brink, A. D. Christianson, D. F. McMorrow

EXPERIMENTAL SETUP AND SAMPLE GEOMETRY

RIXS measurements were performed at the Os L_3 edge ($E = 10.871$ keV) on the ID20 spectrometer at the ESRF, Grenoble. Preliminary measurements were performed at 9-ID-B, Advanced Photon Source. For high resolution measurements a Si (6, 6, 4) channel-cut secondary monochromator was used to select the incident energy. A Si (6, 6, 4) diced spherical analyser (2 m Rowland circle radius) was used to reflect the scattered photons towards a Maxipix CCD detector (pixel size $55 \mu\text{m}$) and discriminate the scattered photon energy. The total energy resolution was determined to be $\Delta E = 56$ meV, based on scattering from a structural Bragg reflection (Fig. S1). A similar value was obtained from diffuse scattering from polypropylene-based adhesive tape (not shown). For low resolution measurements, a similar setup was used, but with a Si (3, 1, 1) channel-cut secondary monochromator instead. The total energy resolution in this case was $\Delta E \approx 300$ meV.

A single crystal of NaOsO_3 (approximate dimensions $0.3 \times 0.3 \times 0.3$ mm³) was oriented such that the (1, 0, 1) direction was normal to the sample surface (Fig. S2). The sample was mounted with silver paint and placed in a custom-made heater setup filled with helium exchange gas. Temperature stability was better than ± 0.5 K. The scattering plane and incident photon polarisation were both horizontal (π -incident polarization) with the incident beam focussed to a size of $20 \times 10 \mu\text{m}^2$ (H \times V) at the sample position.

Four RIXS spectra were collected for each temperature and momentum transfer (30s/pt). These spectra were each normalized to the intensity of the intra- t_{2g} excitations at 1 eV energy loss, cross-correlated to account for any temporal shift in the elastic line position, then averaged. Example spectra are given in Fig. S3. We observed a variation in the elastic line intensity between successive scans at Γ , which was the first point in reciprocal space measured at each temperature. This may be due to local surface reconstruction. Nevertheless, the inelastic features remain consistent between datasets, which means that the current analysis remains valid.

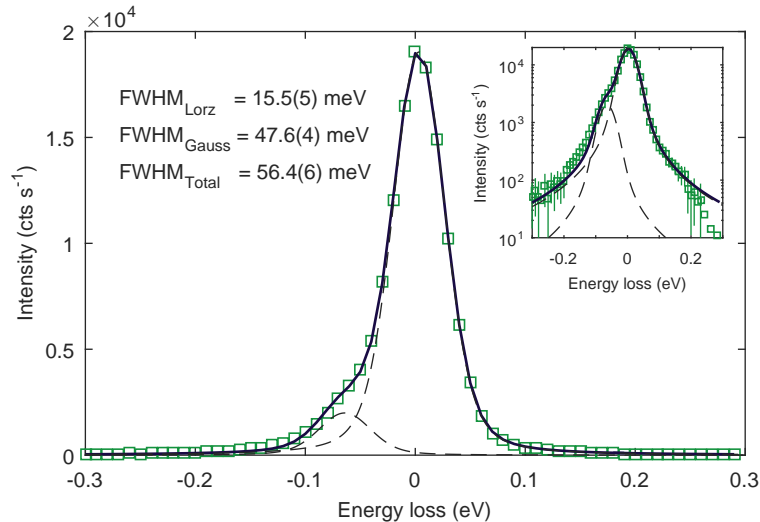


FIG. S1. Spectrometer resolution function for NaOsO_3 obtained at a structural Bragg reflection. Solid line is best fit to sum of two Voigt functions with the same Lorentzian and Gaussian widths. The asymmetry arises due to the fact that $2\theta_A$ is significantly away from 90° at the Os L_3 edge. Inset is the same as the main panel, only on logarithmic axes to highlight the peak tails. This profile was used to fit all of the experimental data.

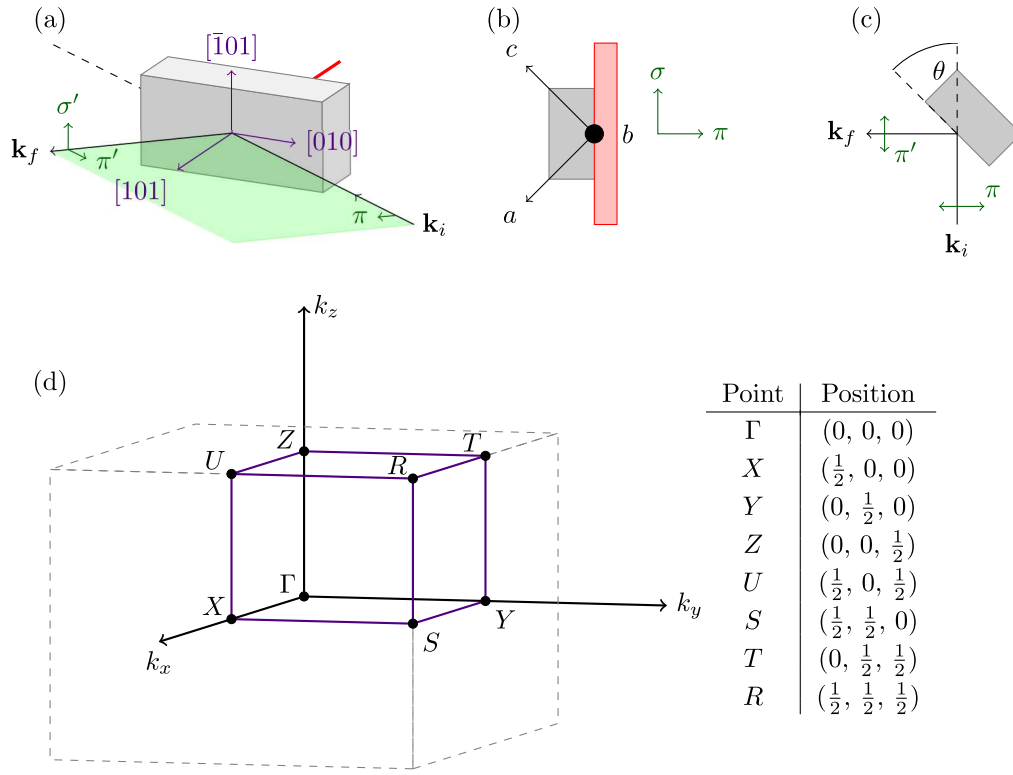


FIG. S2. (a): Schematic of experimental geometry. Magnetic moments lie along the c -axis, the b -axis lies approximately within the scattering plane. (b): View for $\theta = 0$ parallel to the direction of the incident beam. (c): Top-down view. In the experimental geometry $\theta \approx 60^\circ$. (d): Conventional orthorhombic unit cell for the $Pnma$ space group (gray dashed) overlaid with the Brillouin zone (solid purple). Highlighted are the high symmetry points of the Brillouin zone, which are listed in the neighbouring table.

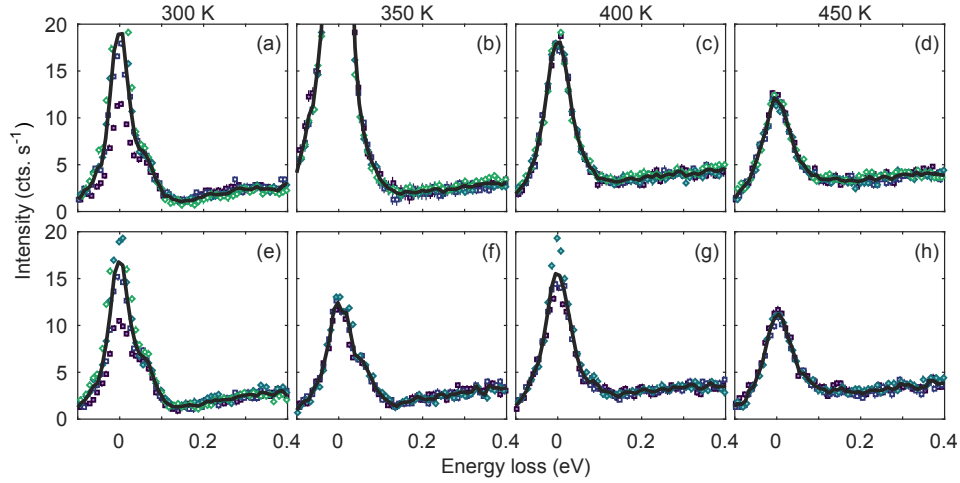
EXPERIMENTAL DATA COLLECTED AT Γ AND Y 

FIG. S3. Raw RIXS spectra collected at Γ as a function of temperature. Different coloured symbols correspond to successive datasets. Solid line is average over all the datasets. (a)–(d): Data collected in first run. The large elastic line (especially at 350 K) is due to an alignment issue. (e)–(h): Data collected in second run, which show a reduced elastic line. The variation in elastic line intensity for successive scans is likely due to local surface reconstruction. Importantly all inelastic features are consistent between datasets.

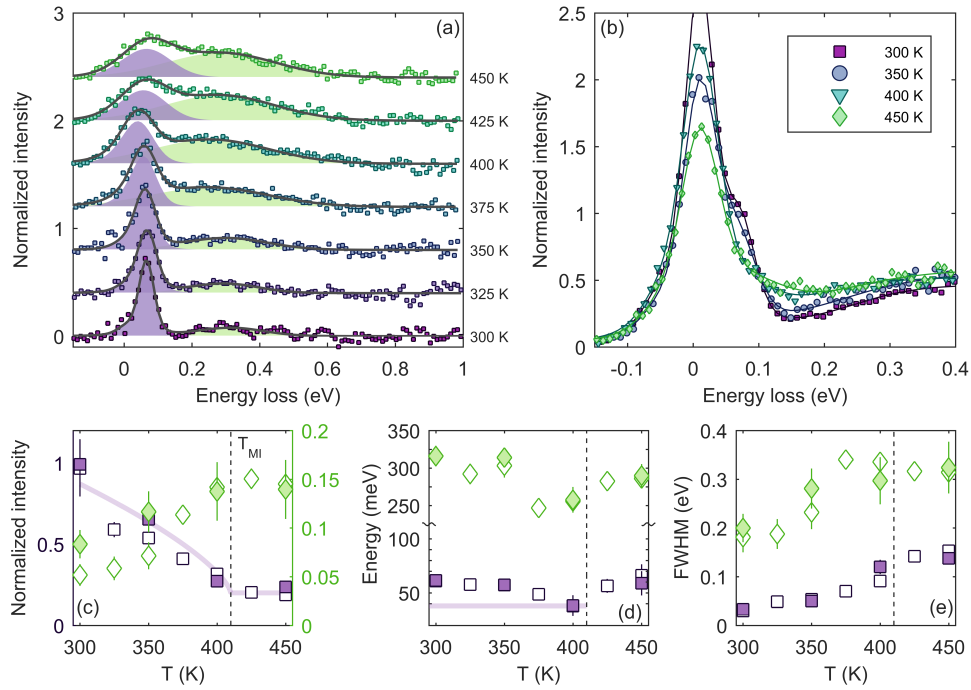


FIG. S4. Analysis of RIXS spectra collected at Γ . (a): Spectra with elastic line and d-d contributions subtracted. Added are the best fit to the data (black solid line), and relative components of the magnon peak (purple) and particle-hole continuum (green). (b): Representative low-energy RIXS spectra, each of which is normalised to the d-d excitations at 1 eV. (c–e): Fitted peak intensity (c), energy (d) and FWHM (e) of the two components as a function of temperature. The two sets of symbols (open or filled) correspond to two separate collection runs. Solid lines are guides to the eye.

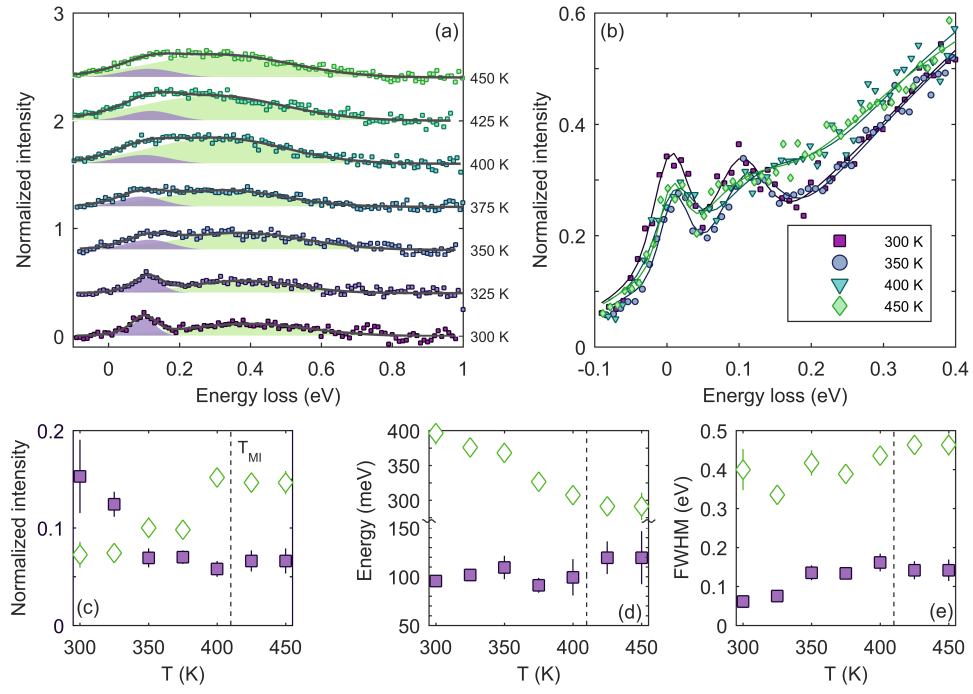


FIG. S5. Analysis of RIXS spectra collected at Y . The layout is the same as for Fig. S4, except that all data was collected over a single run.

CALCULATION OF SINGLE- AND TWO-MAGNON SCATTERING CROSS-SECTIONS

In inelastic neutron scattering, the partial differential scattering cross-section is proportional to the dynamical correlation function $S^{\alpha\alpha}(\mathbf{Q}, \omega)$:

$$S^{\alpha\alpha}(\mathbf{Q}, \omega) = \frac{1}{2\pi\hbar N} \sum_{jj'} e^{i\mathbf{Q}(\mathbf{R}_j - \mathbf{R}_{j'})} \int_{-\infty}^{\infty} dt e^{-i\omega t} \langle S_{j'}^{\alpha}(0) S_j^{\alpha}(t) \rangle, \quad (1)$$

where α indexes the Cartesian direction (x, y, z) of the spin component, N is the total number of spins and the sum runs over all sites j and j' in the lattice. Various theoretical works [1, 2] have shown that the RIXS magnetic cross-section resembles $S(\mathbf{Q}, \omega)$, at least in the case of the single-band Hubbard model at various filling levels. This, at least partly, justifies the use of the following approach to estimate the one- and two-magnon scattering cross-sections as a function of energy and momentum transfer. The authors note, however, that the agreement between the RIXS cross-section and $S(\mathbf{Q}, \omega)$ may not be as complete in the itinerant limit. Calculation of the RIXS cross-section is numerically involved and remains a subject for future study.

Single magnon dispersion and cross-section

The procedure goes as follows. Just as in Ref. 3, the following minimal Hamiltonian was used to model the single magnon mode:

$$\mathcal{H} = J_1 \sum_{nn} \mathbf{S}_i \cdot \mathbf{S}_j + J_2 \sum_{nnn} \mathbf{S}_i \cdot \mathbf{S}_j + \Gamma \sum_{nn,nnn} S_i^z S_j^z. \quad (2)$$

In Eqn 2, the first sum is over nearest neighbours (in the a - c plane), the second sum is over next-nearest neighbours (in the b -direction), and the final term represents an *effective* anisotropy along the c -axis. This latter term parametrizes the contributions from single-ion anisotropy or exchange anisotropy (both symmetric and antisymmetric). A full analysis should include all of these individual terms, however it was not possible to disentangle the relative contributions within the experimental energy resolution. The nearest-neighbour and next-nearest neighbour distances vary only slightly; the difference between them is due to the weak orthorhombic distortion. Thus Equation 2 is in effect an anisotropic nearest-neighbour Hamiltonian. From now on we work in a reference frame where the mean spin direction for each site appears along the z -axis for all sites. For NaOsO_3 this coincides with the laboratory reference frame.

Within linear spin wave theory (LSWT), it is assumed that spin waves occur as a result of fluctuations of the magnetic moment transverse to the ordered spin direction. The spin raising and lowering operators are rewritten in terms of boson annihilation (creation) operators $a_i^{(\dagger)}$ and $b_i^{(\dagger)}$, using a Holstein-Primakoff transformation:

$$\begin{aligned} \mathbf{S}_i^+ &= \sqrt{2S \left(1 - \frac{a_i^\dagger a_i}{2S}\right)} a_i & \mathbf{S}_j^+ &= b_j^\dagger \sqrt{2S \left(1 - \frac{b_j^\dagger b_j}{2S}\right)} \\ \mathbf{S}_i^- &= a_i^\dagger \sqrt{2S \left(1 - \frac{a_i^\dagger a_i}{2S}\right)} & \mathbf{S}_j^- &= \sqrt{2S \left(1 - \frac{b_j^\dagger b_j}{2S}\right)} b_j \\ \mathbf{S}_i^z &= S - a_i^\dagger a_i & \mathbf{S}_j^z &= -S + b_j^\dagger b_j, \end{aligned}$$

where a_i and b_i operate on different magnetic sublattices. In the Holstein-Primakoff approximation, the square root within the spin operators is formally expanded as a Taylor series into powers of $(a_i^\dagger a_i / 2S)$ and $(b_i^\dagger b_i / 2S)$.

Neglecting magnon-magnon interactions, and taking only the leading order terms of the expansion, one obtains the approximate form of the spin operators within LSWT:

$$\begin{aligned} \mathbf{S}_i^+ &\simeq \sqrt{2S} a_i & \mathbf{S}_j^+ &\simeq \sqrt{2S} b_j^\dagger \\ \mathbf{S}_i^- &\simeq \sqrt{2S} a_i^\dagger & \mathbf{S}_j^- &\simeq \sqrt{2S} b_j \\ \mathbf{S}_i^z &= S - a_i^\dagger a_i & \mathbf{S}_j^z &= -S + b_j^\dagger b_j. \end{aligned}$$

Substituting these expressions for the spin operators into the magnetic Hamiltonian (Equation 2), and then diagonalizing through a Bogoliubov transformation, one can determine the magnon dispersion relation and intensities.

The magnon dispersion relation $\omega(\mathbf{Q})$ is given by:

$$\begin{aligned} \omega_{\mathbf{Q}} &= \sqrt{A_{\mathbf{Q}}^2 - B_{\mathbf{Q}}^2} \\ A_{\mathbf{Q}} &= 2S [2J_1 + J_2 + 3\Gamma] \\ B_{\mathbf{Q}} &= 2S [J_1 \cos \pi(h+l) + J_1 \cos \pi(h-l) + J_2 \cos \pi k]. \end{aligned} \quad (3)$$

For a d^3 system like NaOsO₃, one would expect $S = 3/2$. However neutron powder diffraction measurements [4] determined that the effective ordered moment in NaOsO₃ was $\mu_{\text{eff}} = 1.0(1) \mu_{\text{B}}$; reduced from the theoretical moment due to spin-orbit coupling [5]. Using this value for the ordered moment S , one finds $J_1 = J_2 = 21(3)$ meV and $\Gamma = 2.2(4)$ meV. Note that these values differ from those given in Ref. [3], however this is purely due to the value of S used. The spin-wave dispersions in the two cases are otherwise identical, since the exchange parameters are effectively renormalized.

The scattering intensity of the single magnon mode depends on the Bogoliubov operators $u_{\mathbf{Q}}$ and $v_{\mathbf{Q}}$. These were used to diagonalize the Hamiltonian, and are defined as $u_{\mathbf{Q}} = \cosh \theta_{\mathbf{Q}}$ and $v_{\mathbf{Q}} = \sinh \theta_{\mathbf{Q}}$, with $\tanh 2\theta_{\mathbf{Q}} = B_{\mathbf{Q}}/A_{\mathbf{Q}}$. The corresponding transverse spin-spin correlations $S^{xx}(\mathbf{Q}, \omega) = S^{yy}(\mathbf{Q}, \omega)$ are given by [6]:

$$S^{xx}(\mathbf{Q}, \omega) \propto \frac{S - \Delta S^z}{2} [n(\omega_{\mathbf{Q}}) + 1] (u_{\mathbf{Q}} - v_{\mathbf{Q}})^2 \delta(\hbar\omega - \hbar\omega_{\mathbf{Q}}), \quad (4)$$

where $n(\omega_{\mathbf{Q}})$ is the Bose factor, and $\Delta S^z = S - \langle S^z \rangle$ is the spin reduction due to zero-point fluctuations. In the linear spin wave approximation, the spin reduction can be calculated as: $\Delta S^z = (2/N) \sum_{\mathbf{q}} [u_{\mathbf{q}}^2 n(\omega_{\mathbf{q}}) + v_{\mathbf{q}}^2 (n(\omega_{\mathbf{q}}) + 1)]$, where N is the total number of spins, and \mathbf{q} extends over the entire Brillouin zone. In the $T = 0$ limit this expression reduces to $\Delta S = (1/N) \sum_{\mathbf{q}} |v_{\mathbf{q}}^2|$. For NaOsO₃, $\Delta S^z = 0.023$ at $T = 0$, which indicates that quantum fluctuations do not significantly renormalise the spin wave interactions. Such a result is unsurprising given the significant spin wave anisotropy and three-dimensional nature of this nominally $S = 3/2$ system.

Consequently to order ΔS^z the single magnon partial differential cross-section is given by:

$$\left(\frac{d^2 \sigma}{d\Omega dE'} \right)^{(xx)} \propto \frac{S - \Delta S^z}{2} (u_{\mathbf{Q}} - v_{\mathbf{Q}})^2 \{ [n(\omega_{\mathbf{Q}}) + 1] \delta(\hbar\omega - \hbar\omega_{\mathbf{Q}}) + n(\omega_{\mathbf{Q}}) \delta(\hbar\omega + \hbar\omega_{\mathbf{Q}}) \}. \quad (5)$$

The total intensity of the transverse correlations integrated over energy and the entire Brillouin zone is given by $S^{xx}(\mathbf{Q}, \omega) + S^{yy}(\mathbf{Q}, \omega) = (S - \Delta S^z)(2\Delta S^z + 1)$. This fact shall be used later to correctly normalize the relative contributions to the inelastic spectra.

Two magnon cross-section

The longitudinal component of the scattering cross-section $S^{zz}(\mathbf{Q}, \omega)$ has two contributions: an elastic part ($\hbar\omega = 0$), and an inelastic part ($\hbar\omega \neq 0$). These shall be outlined in turn.

Elastic component

The elastic contribution gives the intensity of the magnetic Bragg reflection associated with the time-independent (i.e. non-fluctuating) part of the spin operator \mathbf{S}^z . This component of $S^{zz}(\mathbf{Q}, \omega)$ shall be neglected for now since we are interested in the inelastic processes, but is included for completeness:

$$\left(\frac{d^2\sigma}{d\Omega dE'} \right)_{\hbar\omega=0}^{(zz)} = \delta(\hbar\omega) \frac{(2\pi)^3}{V_m} (S - \Delta S^z)^2 \sum_{\tau} \delta(\mathbf{Q} - (\boldsymbol{\tau} - \boldsymbol{\tau}_{\text{AFM}})), \quad (6)$$

where V_m is the volume of the magnetic unit cell, the sum over τ extends over all structural Bragg reflections and $\boldsymbol{\tau}_{\text{AFM}}$ is the wavevector of any magnetic Bragg reflection. Note that the magnetic propagation vector $\mathbf{q} = 0$ for NaOsO_3 . When integrated over energy and a single Brillouin zone, $S^{zz}(\mathbf{Q}, \omega)_{\text{el}} = (S - \Delta S)^2$.

Inelastic contribution

The inelastic contribution $S^{zz}(\mathbf{Q}, \omega)_{\hbar\omega \neq 0}$ arises due to two-magnon scattering. There are three different types of two-magnon processes: two-magnon creation, two-magnon annihilation, and mixed magnon creation-annihilation. The partial differential two-magnon cross section is equal to the sum of these discrete processes:

$$\left(\frac{d^2\sigma}{d\Omega dE'} \right)_{\hbar\omega \neq 0}^{(zz)} = \left(\frac{d^2\sigma}{d\Omega dE'} \right)_{(aa)}^{(zz)} + \left(\frac{d^2\sigma}{d\Omega dE'} \right)_{(cc)}^{(zz)} + \left(\frac{d^2\sigma}{d\Omega dE'} \right)_{(ca)}^{(zz)} \quad (7)$$

$$\left(\frac{d^2\sigma}{d\Omega dE'} \right)_{(aa)}^{(zz)} \propto \frac{2}{N} \sum_{\mathbf{q}} \frac{1}{2} (u_{\mathbf{q}} v_{\mathbf{q}+\mathbf{Q}} - u_{\mathbf{q}+\mathbf{Q}} v_{\mathbf{q}})^2 \times n(\omega_{\mathbf{q}}) [n(\omega_{\mathbf{q}+\mathbf{Q}}) + 1] \delta(\hbar\omega + \hbar\omega_{\mathbf{q}} + \hbar\omega_{\mathbf{q}+\mathbf{Q}}) \quad (8)$$

$$\left(\frac{d^2\sigma}{d\Omega dE'} \right)_{(cc)}^{(zz)} \propto \frac{2}{N} \sum_{\mathbf{q}} \frac{1}{2} (u_{\mathbf{q}} v_{\mathbf{q}+\mathbf{Q}} - u_{\mathbf{q}+\mathbf{Q}} v_{\mathbf{q}})^2 \times [n(\omega_{\mathbf{q}}) + 1] [n(\omega_{\mathbf{q}+\mathbf{Q}}) + 1] \delta(\hbar\omega - \hbar\omega_{\mathbf{q}} - \hbar\omega_{\mathbf{q}+\mathbf{Q}}) \quad (9)$$

$$\left(\frac{d^2\sigma}{d\Omega dE'} \right)_{(ca)}^{(zz)} \propto \frac{2}{N} \sum_{\mathbf{q}} (u_{\mathbf{q}} u_{\mathbf{q}+\mathbf{Q}} - v_{\mathbf{q}} v_{\mathbf{q}+\mathbf{Q}})^2 \times n(\omega_{\mathbf{q}}) [n(\omega_{\mathbf{q}+\mathbf{Q}}) + 1] \delta(\hbar\omega + \hbar\omega_{\mathbf{q}} - \hbar\omega_{\mathbf{q}+\mathbf{Q}}). \quad (10)$$

At low temperatures only the two magnon creation term (Eqn. 9) contributes significantly to the scattering cross-section, since $n(\omega_{\mathbf{q}}) \approx 0$. At elevated temperatures however the other components also become important. The above expressions are valid if magnon-magnon interactions are neglected. When integrated over energy and a single Brillouin zone, $S^{zz}(\mathbf{Q}, \omega)_{\hbar\omega \neq 0} = \Delta S^z (1 - \Delta S^z) + \langle uv \rangle^2$, where $\langle uv \rangle^2 = \sum_{\mathbf{q}} u_{\mathbf{q}} v_{\mathbf{q}} / N$.

Numerical evaluation of single and two-magnon cross-sections

Consider the simple case of an isotropic 2D Heisenberg antiferromagnet on a square lattice. For a given wavevector, the two magnon continuum extends from the energy of the single magnon, up to twice the zone boundary energy. Notably the spectral weight is concentrated at low energy around the antiferromagnetic Bragg positions at (π, π) , since the single magnon intensity diverges at (π, π) . Inclusion of anisotropy in the Hamiltonian breaks the rotational degeneracy in the ground state; the single magnon dispersion develops a gap, and the intensity no longer diverges at (π, π) . The two-magnon continuum correspondingly no longer has its lower limit at the one-magnon energy, but also develops a gap. Moreover there is a partial redistribution of spectral weight from the magnetic Brillouin zone centre to the rest of the zone. In three dimensions the situation is the same, however the scattering phase space is that much greater. This means that spectral weight tends to be concentrated at the zone boundaries, and hence is considerably

less than dispersive than the 1D and 2D cases.

The single- and two-magnon scattering cross-sections were evaluated numerically for NaOsO₃ using a weighted Monte Carlo method. This approach is similar to that used for the one-dimensional KCuF₃ [7], as well as for the two-dimensional compounds, Cs₂CuF₄ [8] and Cu(DCOO)₂ · 4H₂O [9].

The procedure for calculating the two-magnon cross-section is as follows:

- Choose two random \mathbf{Q} vectors within the three-dimensional Brillouin zone, henceforth defined as \mathbf{Q}_1 and \mathbf{Q}_2 . These correspond to two separate magnon events.
- Evaluate the weight of this process $W_{\mathbf{Q}_1, \mathbf{Q}_2}$ using Eqn. 7.
- Compute the ratio $w = W_{\mathbf{Q}_1, \mathbf{Q}_2} / W_{\mathbf{Q}_1, \mathbf{Q}_2}^{\max}$, where $W_{\mathbf{Q}_1, \mathbf{Q}_2}^{\max}$ is the weight of the most likely event.
- Generate a uniformly distributed random number r between 0 and 1, and compare this to w . If $w < r$, then the event $(\mathbf{Q}_1, \mathbf{Q}_2)$ is accepted. Otherwise it is rejected.
- In the case that the event is accepted, then calculate the total energy $\hbar\omega_{\text{tot}} = \hbar\omega_{\mathbf{Q}_1} + \hbar\omega_{\mathbf{Q}_2}$ and total wavevector $\mathbf{Q}_{\text{tot}} = \mathbf{Q}_1 + \mathbf{Q}_2$. If \mathbf{Q}_{tot} lies outside the first Brillouin zone, then it is folded back via subtraction of a reciprocal lattice vector \mathbf{G} .

This process is repeated until a large number of events are accepted. For NaOsO₃, 1×10^9 iterations were performed in order to generate $S^{xx(yy)}(\mathbf{Q}, \omega)$, and $S^{zz}(\mathbf{Q}, \omega)$ as a function of momentum transfer and energy. These functions were then normalised by $(S - \Delta S^z)(2\Delta S^z + 1)$ and $\Delta S^z(1 - \Delta S^z) + \langle uv \rangle^2$ respectively, in order to obtain a direct comparison with experiment.

The experimental geometry governs the relative contributions of $S^{xx}(\mathbf{Q}, \omega)$, $S^{yy}(\mathbf{Q}, \omega)$, and $S^{zz}(\mathbf{Q}, \omega)$ to the scattering cross-section. It is reiterated that this may not be equal to the RIXS cross-section, as orbital effects for example are neglected. Haverkort [1] proposed a simple selection rule for the measurement of single spin-flip excitations (magnons) with RIXS: Magnons can be observed with cross-polarised light for spins in the plane of the polarisation. We have almost entirely π -incident polarization (undulator source), which means that the incoming X-rays are polarized parallel to the scattering plane. The cross-polarized channel lies perpendicular to the scattering plane, given the notation σ in line with current convention. Consequently we observe those spin components which lie within the π' - σ' polarization plane, with the primes denoting the polarization of the scattered beam. For the present scattering geometry, the intensity is approximately given by the relation:

$$I \propto S^{yy}(\mathbf{Q}, \omega) \cos \theta + \sqrt{2} \sin \theta [S^{xx}(\mathbf{Q}, \omega) + S^{zz}(\mathbf{Q}, \omega)], \quad (11)$$

where the angle θ is defined by the rotation of the sample within the scattering plane. A small momentum-dependent tilt out of the scattering plane by $< 4^\circ$ has been neglected; this contributes only weakly to the intensity.

The results of this simulation are plotted in Fig. S6(a), assuming no spin wave damping. A clear dispersive mode can be observed between 60 and 130 meV, along with a broad continuum of states which extends up to 260 meV. These correspond to the single and two-magnon excitations respectively. Anisotropy not only induces a gap in the single magnon dispersion, but also acts to separate the single and two-magnon excitations. From Fig. S6a, it appears that the two magnon continuum is most concentrated at the zone boundaries, as expected.

Clearly the simulations qualitatively reproduce the expected behaviour for both the single magnon and two magnon continuum. Quantitative comparisons are provided in Figs. S6(b,c) at Γ and Y . The relative intensities of the single magnon peak at different momentum transfers are well described by the Monte Carlo simulation. On the other hand, the high energy spectral weight cannot be fully modelled in terms of this simple model for the two-magnon continuum. There are however two factors which have not been considered thus far that help to explain the discrepancy.

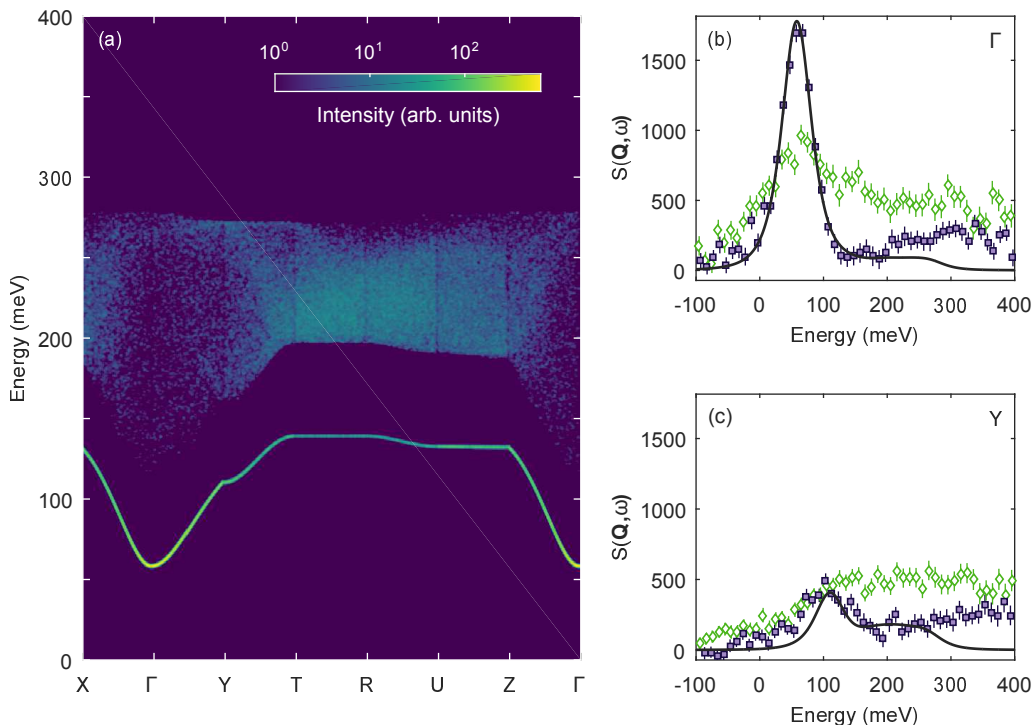


FIG. S6. (a): Transverse $[S^{xx}(\mathbf{Q}, \omega)]$ and longitudinal $[S^{zz}(\mathbf{Q}, \omega)]$ spin-spin correlation functions, calculated as a function of energy and momentum transfer. The simulation ran over 1×10^9 Monte Carlo steps, with each displayed single and two-magnon event broadened by a two-dimensional Gaussian with FWHMs 0.5 meV and 0.01 reciprocal lattice units (r. l. u.) for clarity. No spin wave damping has been assumed. All Bose factors have been calculated assuming $T = 300$ K. Lines at high symmetry points are artefacts of the plotting routine. (b, c): Comparison of the $S(\mathbf{Q}, \omega)$ calculations (solid line) with uniformly scaled experimental RIXS data at Γ (b) and Y (c). Filled squares refer to data obtained at 300 K, open diamonds to data obtained at 450 K. The calculated $S(\mathbf{Q}, \omega)$ has been convoluted with a Pearson VII function of FWHM 56 meV and profile parameter $\mu = 2$, in order to represent the effect of the instrumental resolution. Note that this does not include the effect of the finite momentum resolution of the spectrometer. The RIXS data has had the elastic and $d-d$ contributions subtracted, in order to highlight the remaining features.

The first is that the calculations assume a purely localised model (Heisenberg), and do not include the effect of spin wave damping. At 300 K, the charge gap in NaOsO_3 is approximately 80 meV [10]. Consequently one may expect that above this threshold, the magnons become Landau damped due to scattering from an intraband electron-hole continuum of states. This hypothesis is partly justified by the observation that the Monte Carlo simulations seem to slightly underestimate the experimental peak width of the zone boundary (Y) single magnon peak at 100 meV. Such an effect would also likely apply to the two-magnon excitations.

The second factor is that the experimental RIXS spectra are the average over all outgoing polarisation channels. This means that they not only include contributions from the cross-polarised $\pi-\sigma'$ channel, but also from the $\pi-\pi'$ channel. The $\pi-\pi'$ channel contains all non-magnetic scattering components, including electronic excitations. If the charge gap is small, then one may observe charge scattering from a broad continuum of (weakly momentum-dependent) interband particle-hole excitations. Such an effect has been previously observed via RIXS in Na_2IrO_3 [11], and may partly be the origin for the high-energy scattering beyond 0.3 eV. Note that any excitonic behaviour (if present) is likely to be hidden by the single-magnon peak at a similar energy.

INTER-BAND TRANSITIONS

In order to test the validity of this prediction, we performed calculations of potential dipole-allowed inter-band transitions for NaOsO₃. The starting point was the band structure calculated by Bongjae Kim and colleagues at T_N (Fig. 3c in Ref. [12]). To simplify matters we only consider the two bands closest to the Fermi energy, which were fitted within the parabolic band approximation:

$$E(\mathbf{k}) = \frac{\hbar}{2} \left[\frac{(k_x - k_{x,0})^2}{m_x^*} + \frac{(k_y - k_{y,0})^2}{m_y^*} + \frac{(k_z - k_{z,0})^2}{m_z^*} \right] + E_0, \quad (12)$$

where $m_{x,y,z}^*$ refers to the effective mass in the respective Cartesian direction, and E_0 is the energy at the band minimum located at $(k_{x,0}, k_{y,0}, k_{z,0})$. This was assumed to be at Y . The band energies at high symmetry points (as calculated by Kim) were used to constrain the fits. The results of this fit are displayed in Fig. S7b, with all the main features of the two electronic bands reasonably reproduced.

Fig. S7a shows the results of a Monte Carlo simulation performed over 5×10^8 events. The general method was similar to that used to calculate the one- and two-magnon cross-section. A broad, weakly momentum dependent, continuum can be observed around 0.3 eV energy loss, which is of a similar scale to the high energy peak observed in the RIXS data. This fits with the hypothesis that there may indeed be an intrinsic electronic component present within the RIXS data.

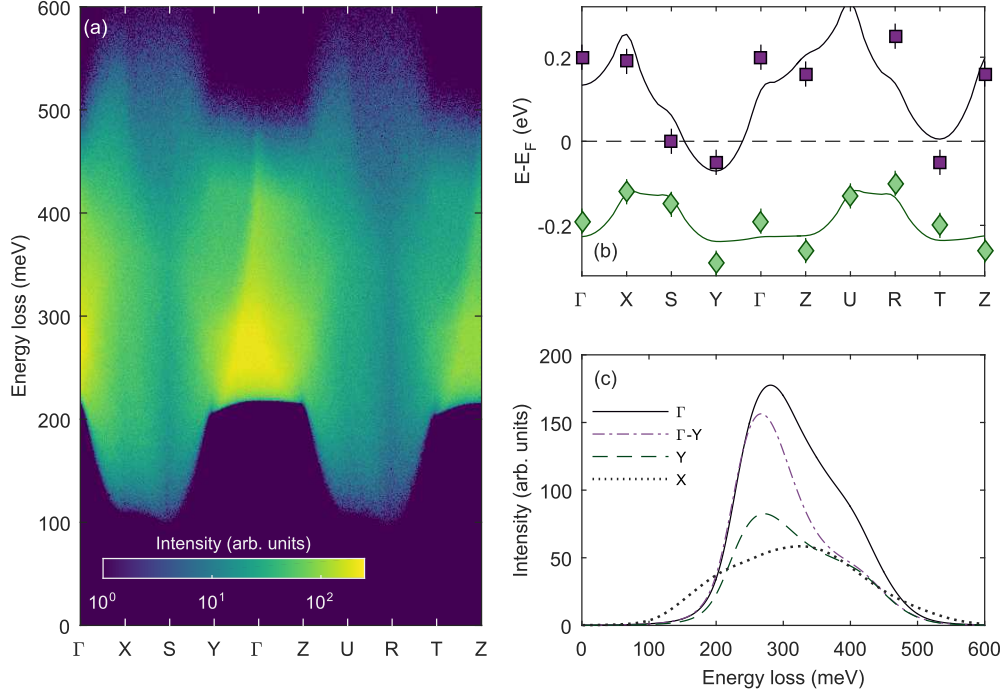


FIG. S7. Calculation of dipole-allowed interband transitions for NaOsO₃. (a): Results of Monte Carlo simulation (5×10^8 events) shown for a portion of the Brillouin zone. (b): Theoretical band structure of NaOsO₃ at T_N , as calculated within Ref. 12. Symbols indicate values at high symmetry points extracted from manuscript, with error bars reflecting the uncertainty in this procedure. Solid lines are results of fits to this band structure within the parabolic approximation. The main features of the band structure are reproduced. Fitting parameters $[m_x^*, m_y^*, m_z^*, E_0]$ for conduction band: $[0.8(2), 2.4(3), 0.4(2), -0.07(3)$ eV]; for valence band: $[0.6(2), 0.1(3), 0.0(2), -0.24(3)$ eV]. All effective masses are given in units of m_e . (c): Cuts of data presented in (a), taken at various reciprocal lattice points as indicated. The effect of the instrumental energy resolution has been included.

However, this conclusion suffers from a number of limitations. Fundamentally, RIXS at the L_3 edge is not a direct probe of the band structure, even in weakly correlated systems. We note that K-edge (indirect) RIXS can measure the band structure through the joint density of states (JDOS), with a more detailed discussion given in Refs. [13] and [14]. Unfortunately the Os K-edge lies at 73.9 keV, which is well above the present capabilities of any currently available RIXS instrumentation. Secondly we only considered transitions between the two bands closest to the Fermi level; there are likely to be additional contributions to the observed scattering from neighbouring bands. Moreover the calculated band structure has not been verified experimentally (via photoelectron emission spectroscopy for example), and contains a degree of fine structure which has been averaged out within the present analysis. The amplitude of the calculated interband transitions appears to decrease by a factor of two at the zone boundary (Y), compared to the zone centre (Γ). This is not observed in the RIXS data (compare with Figs. S4c and S5c), however note that the finite momentum resolution of the spectrometer has not been taken into account when performing the interband calculations. Finally the energy scale of the continuum is considerably larger than kT_N . We hence expect the scattering intensity to vary little with temperature, provided that the temperature change is not too large. This is at apparent odds with the experimentally observed behaviour.

CALCULATION OF MICROSCOPIC PARAMETERS

The magnitudes of Hund's coupling J_H and the one-electron spin-orbit coupling parameter ζ can be estimated from the energies of the electronic transitions in the RIXS spectra. The starting point is a single Os^{5+} cation octahedrally coordinated to six O^{2-} ions, assuming no distortion away from ideal octahedral symmetry. For NaOsO_3 this is not strictly true, however the distortion is sufficiently small ($D\tau/Dq \approx -0.01$) that this approximation holds within experimental resolution. Assuming a spherically symmetric Coulomb interaction, and t_{2g} electronic wavefunctions obtained from crystal field theory which have pure d -character (i.e no hybridisation), then the Hund's coupling J_H can be expressed in terms of the Racah parameters: $J_H = 3B + C$. The Racah parameters can be directly related to Slater integrals using standard transformations: $A = F_0 - 49F_4$, $B = F_2 - 5F_4$, $C = 35F_4$. If only differences between levels are considered, then A cancels out from all expressions. We attempted to estimate J_H and ζ by fitting the orbital excitations in high-resolution ($\Delta E = 56$ meV) RIXS within two limits: Russell-Saunders (LS) coupling and intermediate coupling. These are discussed in more detail below.

LS-coupling limit

In the Russell-Saunders limit (LS -coupling), spin-orbit coupling acts as a perturbation to the electronic Hamiltonian, however is assumed to be weaker than the Coulomb repulsion. Consequently, in the strong field limit, the hierarchy of energy scales follows $10Dq > B, C > \zeta$. Coulomb repulsion within the t_{2g} and e_g manifolds splits them into a series of terms, which are then split further by spin-orbit coupling into energy levels which are Kramers degenerate. These are illustrated in Fig. S8(a) and (b).

Recall that the RIXS spectrum contains a broad peak centred at 1 eV energy loss (peak A), which was indexed as excitations within the t_{2g} manifold. As discussed in the main text, peak A results from the superposition of two peaks centered at $3J_H$ and $5J_H$ respectively in the LS -coupling limit. By fitting the high-resolution RIXS data shown in Fig. S9, we determine $J_H = 0.26(2)$ eV. This agrees with the value obtained from the low resolution RIXS data, and compares well to the previous estimate by Taylor [15] for the isoelectronic d^3 materials $\text{Ca}_3\text{LiOsO}_6$ and Ba_2YOsO_6 .

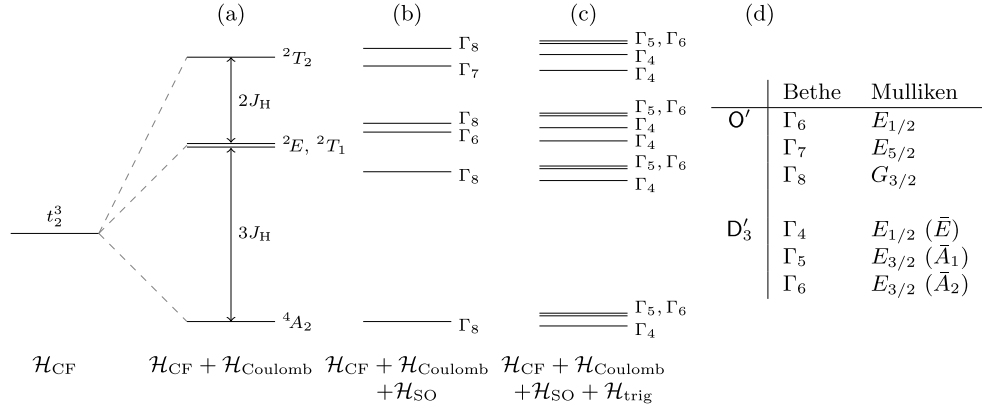


FIG. S8. (a): Terms of a t_2^3 configuration in a first (strong field) approximation, including the effect of Coulomb repulsion. Spin-orbit coupling and distortions away from an ideal octahedral geometry are neglected. The Hund's coupling J_H is equivalent to $3B + C$, where B and C are Racah parameters. The terms 2E and 2T_1 are accidentally degenerate. (b): Electronic fine structure levels obtained when spin-orbit coupling is added as a weak perturbation. Levels are calculated by decomposition of the direct product $\Gamma \times D^{(3/2)}$, and are Kramers degenerate. The separation between levels originating from 2E and 2T_1 is exaggerated for clarity. (c): Addition of a weak trigonal perturbative field to the case presented in (b). Note that the 4A_2 ground state is only split (zero field splitting) by a combination of spin-orbit coupling and trigonal distortion, and even then third-order perturbations are required. (d): Equivalent representations given in the Bethe and Mulliken systems for the O' and D'_3 double groups.

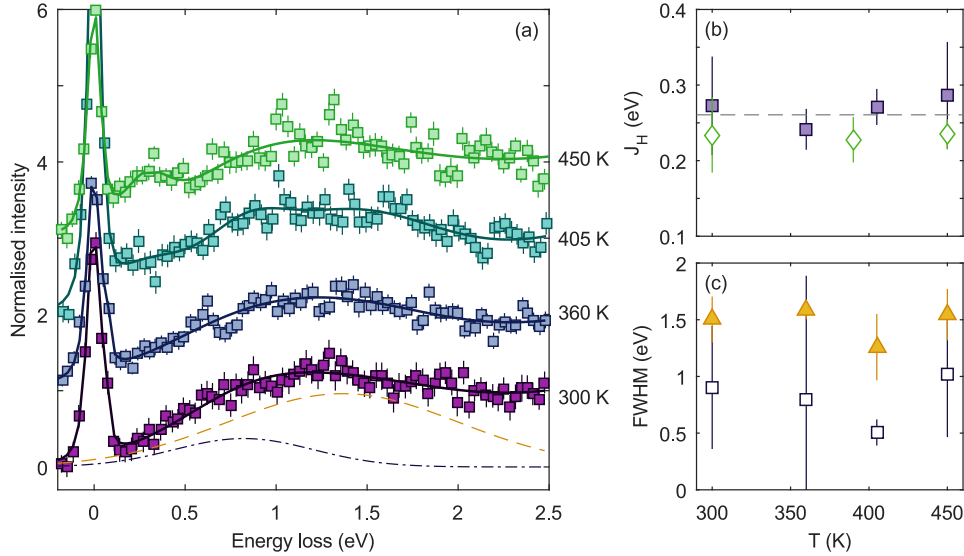


FIG. S9. (a): High-resolution RIXS spectra ($\Delta E = 56$ meV) obtained as a function of temperature close to Γ (5.05, 3.05, 4.05). Solid line is best fit to data using the LS -coupling model described in the main text. Dot-dashed and dashed lines reflect the individual contributions to peak A at $3J_H$ and $5J_H$ respectively. (b): Fitted parameter J_H as a function of temperature using a high-resolution (filled squares) setup. Superimposed is the result using a low-resolution setup (open diamonds). (c): Full width at half maximum (FWHM) of peaks at $3J_H$ (open squares) and $5J_H$ (filled triangles).

Intermediate coupling approach

Within an intermediate coupling approach, spin-orbit coupling and Coulomb repulsion are treated on equal footing. Consequently the hierarchy of interactions goes as $10Dq > \zeta \sim B, C$. The electronic energy levels can be determined from diagonalizing the total energy matrix comprising the various interactions. The general method and interaction matrices used are described within Ref. 16, and is similar to that used by Taylor *et al.* [15]. As shown in Fig. S8b, inclusion of spin-orbit coupling and Coulomb repulsion in the electronic Hamiltonian leads to six Kramers degenerate energy levels emerging from the t_{2g} manifold. Trigonal distortions away from ideal octahedral symmetry result in further separation of these levels (Fig. S8c).

Taylor *et al.* performed RIXS measurements on $\text{Ca}_3\text{LiOsO}_6$ and Ba_2YOsO_6 . These materials show four resolution limited ($\Delta E = 150$ meV) peaks, corresponding to excitations from the ground state (Γ_8) to spin-orbit coupled levels Γ_i within the t_{2g} manifold. Strictly speaking there should be five excitations, however for small values of B two of these excitations appear quasi-degenerate. By fitting the RIXS spectra within an intermediate coupling model, they were able to extract estimates of the Hund's coupling $J_H = 3B + C$ [17], and the single electron spin-orbit coupling parameter ζ . They found that $J_H = 0.3(2)$ eV and $\zeta = 0.32(6)$ eV for Ba_2YOsO_6 , with the significant uncertainty in J_H arising predominantly from C .

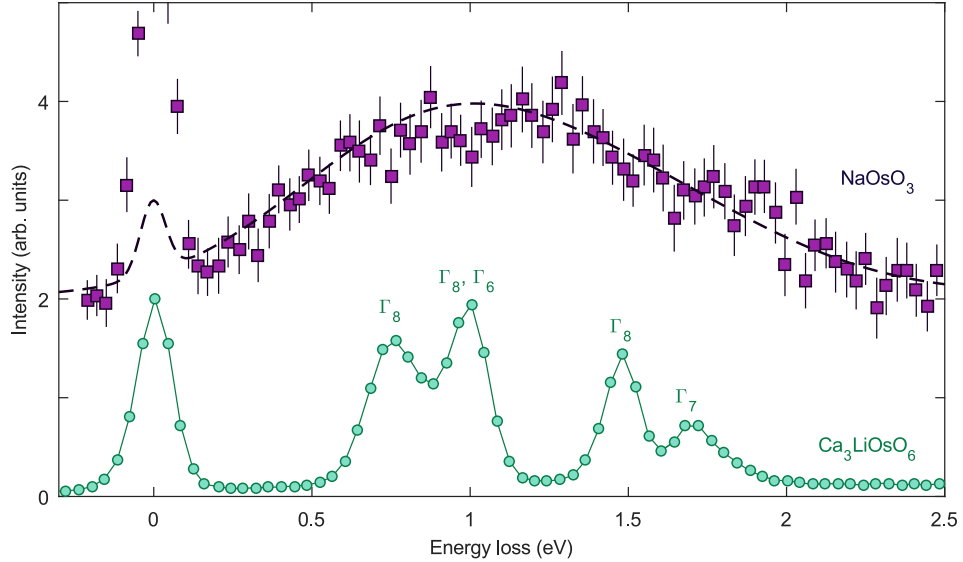


FIG. S10. Comparison of intra- t_{2g} excitations in d^3 osmates. Squares: 300 K RIXS spectrum of NaOsO_3 obtained at Γ . The high energy peaks B and C have been subtracted from the data. Circles: RIXS spectrum of $\text{Ca}_3\text{LiOsO}_6$ (from Ref. [15]), which was collected on a powder with a lower energy resolution ($\Delta E = 150$ meV). The purple dashed line is the spectrum obtained by replacing the four higher energy peaks Γ_i by Gaussians of FWHM 1 eV, whilst keeping their relative amplitudes the same. The good agreement of this curve with the NaOsO_3 data suggests J_H and ζ are similar for the two materials.

We attempted to apply the same method for NaOsO_3 . Unlike $\text{Ca}_3\text{LiOsO}_6$ and Ba_2YOsO_6 however, the intra- t_{2g} excitations are contained within a single, broad peak. The fundamental reason for this is the increased itineracy in NaOsO_3 , and a corresponding reduced lifetime of the core hole in the intermediate state. Consequently each excitation from the ground state to an excited state Γ_i is broad in energy. Moreover, weak distortions away from octahedral symmetry for NaOsO_3 effectively broaden the excitations even further. Even by applying a number of constraints to reduce the parameter space (only consider four excitations, ideal octahedral symmetry, fixed peak width, fix C/B), values of J_H and ζ were obtained which deviate significantly from previous studies on $5d^3$ materials: $J_H = 0.20(2)$ eV, $\zeta = 0.46(2)$ eV. We note that these values are similar to those obtained by Yuan [18] for Sr_2YIrO_6 ($5d^4$), however their simple model neglects the effect of mixing between the t_{2g} and e_g orbitals.

Yet there is a fundamental problem with applying any sort of ligand field model to NaOsO_3 , or more broadly speaking, any system which has intrinsic itineracy. Calculating the effect of Coulomb repulsion involves the evaluation of matrix elements such as $\langle t_{2g}^3 {}^4A_2 | \mathcal{H} | t_{2g}^3 {}^4A_2 \rangle$ for each of the symmetry allowed terms [19]. These matrix elements simplify into combinations of Coulomb and exchange two-electron integrals, historically denoted by J and K respectively. However these integrals can only, strictly speaking, be expressed in terms of Racah parameters A, B, C – or equivalently Slater integrals F_0, F_2, F_4 – if the t_{2g} and e_g many-electron wavefunctions have pure d -character. This point was briefly touched upon earlier. Density functional theory (DFT) calculations by Jung *et al.* [20] attributed an effective 4.3 electrons throughout the valence d -orbitals, instead of the formal 3. This is a direct result of significant hybridisation between the osmium $5d$ and oxygen $2p$ orbitals. Consequently the many-electron wavefunctions no longer have pure d -character, and the assumptions made within ligand field theory break down. This may explain some of the differences in the fitted values of the microscopic parameters, compared to the considerably more localized $\text{Ca}_3\text{LiOsO}_6$ and Ba_2YOsO_6 .

-
- [1] M. W. Haverkort, Phys. Rev. Lett. **105**, 167404 (2010).
- [2] C. Jia, E. Nowadnick, K. Wohlfeld, Y. Kung, C. C. Chen, S. Johnston, T. Tohyama, B. Moritz, and T. Devereaux, Nature Communications **5**, 3314 (2014).
- [3] S. Calder, J. G. Vale, N. Bogdanov, C. Donnerer, D. Pincini, M. Moretti Sala, X. Liu, M. H. Upton, D. Casa, Y. G. Shi, Y. Tsujimoto, K. Yamaura, J. P. Hill, J. van den Brink, D. F. McMorrow, and A. D. Christianson, Phys. Rev. B **95**, 020413 (2017).
- [4] S. Calder, V. Garlea, D. McMorrow, M. Lumsden, M. B. Stone, J. Lang, J.-W. Kim, J. Schlueter, Y. Shi, K. Yamaura, Y. S. Sun, Y. Tsujimoto, and A. D. Christianson, Phys. Rev. Lett **108**, 257209 (2012).
- [5] H. Matsuura and K. Miyake, J. Phys. Soc. Jpn. **82**, 073703 (2013).
- [6] This is true for the minimal Hamiltonian given by Eqn. 2. However if the Dzyaloshinskii-Moriya (DM) interaction is non-zero, then $S^{xx}(\mathbf{Q}, \omega) \neq S^{yy}(\mathbf{Q}, \omega)$. It was previously noted in Ref. [3] that a finite DM interaction is required by symmetry for NaOsO_3 .
- [7] D. A. Tennant, S. E. Nagler, D. Welz, G. Shirane, and K. Yamada, Phys. Rev. B **52**, 13381 (1995).
- [8] R. Coldea, D. A. Tennant, and Z. Tylczynski, Phys. Rev. B **68**, 134424 (2003).
- [9] N. B. Christensen, *Neutron scattering studies of two-dimensional antiferromagnetic spin fluctuations in insulating and superconducting $S = \frac{1}{2}$ systems*, Ph.D. thesis, Risø National Laboratory, Denmark (2003).
- [10] I. L. Vecchio, A. Perucchi, P. Di Pietro, O. Limaj, U. Schade, Y. Sun, M. Arai, K. Yamaura, and S. Lupi, Scientific Reports **3**, 2990 (2013).
- [11] H. Gretarsson, J. P. Clancy, Y. Singh, P. Gegenwart, J. P. Hill, J. Kim, M. H. Upton, A. H. Said, D. Casa, T. Gog, and Y.-J. Kim, Phys. Rev. B **87**, 220407 (2013).
- [12] B. Kim, P. Liu, Z. Ergönenc, A. Toschi, S. Khmelevskiy, and C. Franchini, Phys. Rev. B **94**, 241113 (2016).
- [13] J. P. Hu, D. J. Payne, R. G. Egdell, P.-A. Glans, T. Learmonth, K. E. Smith, J. Guo, and N. M. Harrison, Phys. Rev. B **77**, 155115 (2008).
- [14] Y.-J. Kim, J. P. Hill, H. Yamaguchi, T. Gog, and D. Casa, Phys. Rev. B **81**, 195202 (2010).
- [15] A. E. Taylor, S. Calder, R. Morrow, H. L. Feng, M. H. Upton, M. D. Lumsden, K. Yamaura, P. M. Woodward, and A. D. Christianson, Phys. Rev. Lett. **118**, 207202 (2017).
- [16] J. C. Eisenstein, J. Chem. Phys. **34**, 310 (1961).
- [17] Note that $J_H = 3B + C$ is only correct for coupling within the t_{2g} manifold; the Hund's coupling for electrons between t_{2g} and e_g orbitals, or within the e_g manifold, is given by $J_H = 4B + C$ [19].
- [18] B. Yuan, J. P. Clancy, A. M. Cook, C. M. Thompson, J. Greedan, G. Cao, B. C. Jeon, T. W. Noh, M. H. Upton, D. Casa, T. Gog, A. Paramekanti, and Y.-J. Kim, Phys. Rev. B **95**, 235114 (2017).
- [19] S. Sugano, Y. Tanabe, and H. Kamimura, *Multiplets of Transition-Metal Ions in Crystals*, Pure and Applied Physics (Academic Press, New York, 1970).
- [20] M.-C. Jung, Y.-J. Song, K.-W. Lee, and W. E. Pickett, Phys. Rev. B **87**, 115119 (2013).